Diaphragm-free fiber-optic Fabry–Perot interferometer based on tapered hollow silica tube

CrossMark

Guocheng Fang [a,b], Pinggang Jia [a,b], Ting Liang [a,b], Qiulin Tan [a,b], Yingping Hong [a,b], Wenyi Liu [a,b], Jijun Xiong [a,b,*]

[a] Key Laboratory of Instrumentation Science & Dynamic Measurement, Ministry of Education, North University of China, Taiyuan 030051, China
[b] Science and Technology on Electronic Test & Measurement Laboratory, North University of China, Taiyuan 030051, China

ARTICLE INFO

ABSTRACT

A miniature fiber-optic Fabry–Perot interferometer fabricated by splicing a diaphragm-free hollow silica tube to a single-mode fiber and fusing the inner core to a taper is presented. The tapered zone forces lights to propagate from the fiber core into the silica tube, and the lights is reflected from the end faces of the optical fiber and the hollow silica tube. The contrast ratio of the interference fringe is determined by the minimum inner diameter of hollow silica tube. The responses of the proposed interferometer to high-temperature, gas refractive index, liquid refractive index and pressure were measured and were found to be linear with sensitivities of 16.26 pm/°C, 610.47 nm/RIU, -122.36 dB/RIU and 1.56 pm/kPa, respectively.

1. Introduction

Fiber-optic Fabry–Perot interferometers (FPIs) have been widely used in various sensing applications for temperature [1], pressure [2], strain [3], refractive index (RI) [4], humidity [5], vibration [6], and so on, because of their unique advantages such as simple structure, immunity to electromagnetic interference, high sensitivity, and compact size. A typical FPI consists of a cavity formed by two parallel reflective facets. Multiple reflections and transmissions occur within the cavity and create interference fringes. The traditional method of producing an FPI is to place two well-cut fibers in a hollow silica tube (HST) to form an air gap [7]. With the development of technology, a considerable number of methods have been applied to fabricate miniature FPIs, for example, microelectromechanical systems (MEMS) [8], chemical etching [9], arc discharge [10], lasing [4], applying special optical fibers [11], coating films [5], and so on.

A diaphragm-free fiber-optic FPI has features such as compact structure, simple fabrication process, and bare reflective surfaces, which can generally be fabricated by designing holes on the optical fiber end through chemical etching [9] or by applying special optical fibers [12,13]. Some other novel diaphragm-free FPI structures are also fabricated by combining the two methods or applying some special means [14–16]. Huang et al. were the first to present the idea of a diaphragm-free FPI. They spliced an HST to the tip of a single-mode fiber (SMF) and described the principle of the proposed FPI [17]. Frazao et al. fabricated two types of gas refractometers: one by splicing an HST with a core diameter of 20 μm to an SMF [18], and the other by splicing a silica rod with a large offset between two SMFs [19]. The operating principle was explained by the interference between the core and cladding modes, and the contrast ratio of the interference fringes was influenced by the FPI cavity length. Furthermore, its contrast ratio was as small as 2–3 dB. Wang et al. proposed a gas refractometer with a sensitivity of 441 nm/RIU by etching a concave well on the fiber end; furthermore, they determined the cross-sensitivity coefficient with temperature [20]. The contrast ratio of the interference fringe was also small and the length of the maximum FPI cavity may be limited by the fabrication method.

In this paper, we present an FPI based on a tapered HST, which was fabricated by splicing an HST with an inner diameter of 22 μm and an outer diameter of 125 μm to the end of an SMF and fusing the inner core of the HST to a taper. The tapered inner core forces lights to propagate from the optical fiber core into the HST, which improving the intensity and contrast ratio of the interference fringes. The fabrication process involves only cleaving and arc discharge, which have advantages of low cost and ease of fabrication.

* Corresponding author at: Key Laboratory of Instrumentation Science & Dynamic Measurement, Ministry of Education, North University of China, Taiyuan 030051, China.
E-mail address: xiongjijun@nuc.edu.cn (J. Xiong).
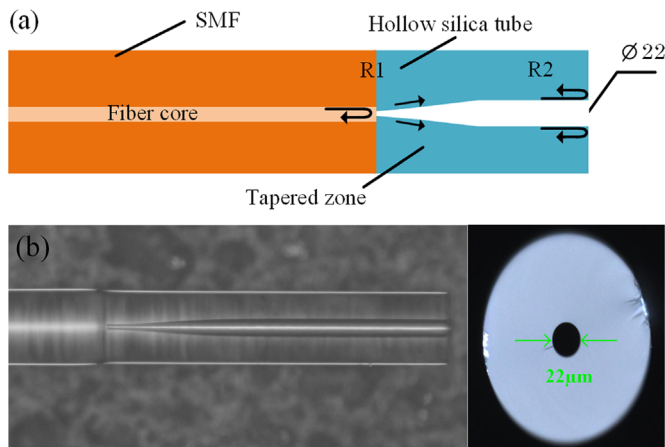
Fig. 1. Structure of fiber-optic FPI: (a) schematic (b) longitudinal and cross-sectional microscopy images.

2. Fiber-optic FPI fabrication

The structure of the fiber-optic FPI and the longitudinal and cross-sectional microscope images are illustrated in Figs. 1(a) and (b), respectively. According to Fig. 1(a), when lights propagates along the SMF, one portion of lights in the optical fiber core is reflected at the reflective facet (R1), and the other portion of lights propagates into the HST and is reflected at the end (R2). The two parts of the reflected lights interfere in the SMF and form the interference fringes. According to Fig. 1(b), the inner diameter of the HST measured by the microscopy image is approximately 22 μm, and the inner air core of the HST is tapered.

The fabrication process for the FPI is as follows. First, a well-cut SMF (Coring SMF-28, 9/125 μm) and an HST are spliced together through arc discharge by a fusion splicer (FITEL, S183 version 2, Japan) at an appropriate fusion intensity and duration. Second, the HST is cut off at an appropriate distance from the fusion joint. Due to thermal fusion, the inner core of the HST collapses and the inner diameter decreases. The shorter the distance from the fusion joint is, the more the inner diameter decreases. Thus, the inner core of the HST becomes tapered. The minimum inner diameter of the taper depends on the intensity and duration of fusion. The minimum inner diameter is equal to nearly half the diameter of the
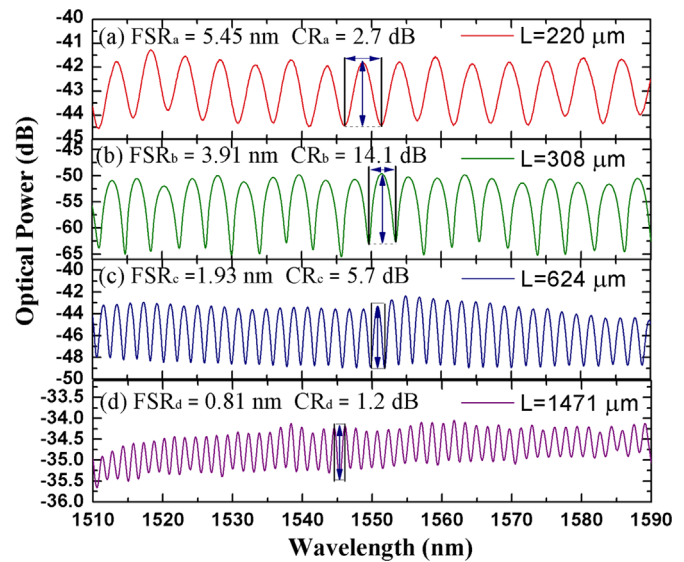
Fig. 3. Interference fringes of FPIs with minimum inner diameters of approximately (a) 2 μm, (b) 5 μm, (c) 7 μm and (d) 14 μm.

fiber core when the initial and final intensities are 100 units and 40 units, respectively, and the duration is 650 ms. In contrast, the minimum inner diameter of the taper becomes smaller or larger than half the diameter of the fiber core on increasing or decreasing fusion intensity or duration, respectively.

Fig. 2 shows photographs of the FPIs with different tapered zones under different intensities and durations of fusion discharge. According to Fig. 2(a)–(d), the minimum inner diameters of the HSTs are approximately 2 μm, 5 μm, 7 μm, and 14 μm, respectively. The interference fringes of the FPIs with minimum inner diameters of approximately 2 μm, 5 μm, 7 μm and 14 μm were obtained using the optical sensing analyzer (Micron Optics Inc., SM125, America), and are shown in Fig. 3(a)–(d) respectively. According to Fig. 3, the contrast ratio varies from approximately 2–14 dB, which can be adjusted by varying the minimum inner diameters of the HST. As shown in Fig. 2(b), when the minimum inner diameter of the HST is approximately 5 μm, the reflected light intensity from R1 is almost equal to that from R2, which leads to high contrast ratio, as shown in Fig. 3(b). Conversely, when the minimum inner diameter
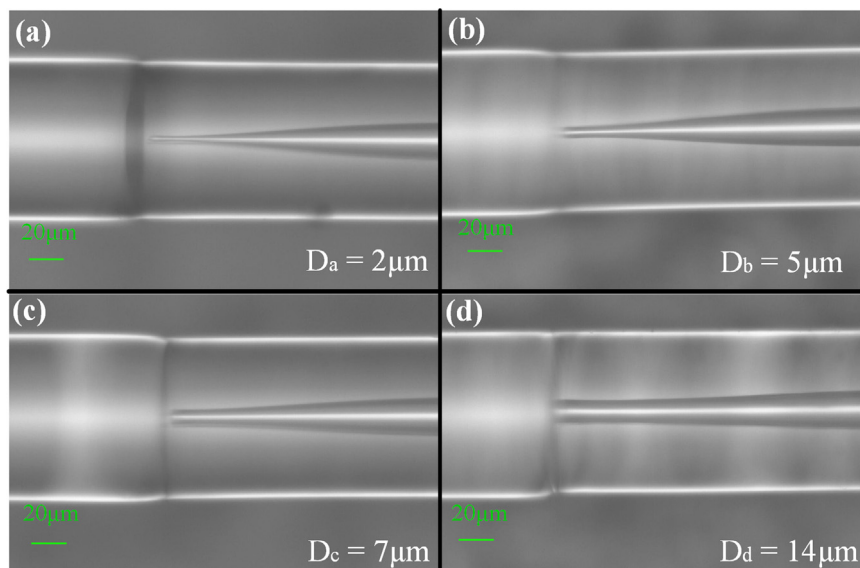
Fig. 2. Photographs of FPIs with minimum inner diameters of approximately (a) 2 μm, (b) 5 μm, (c) 7 μm, and (d) 14 μm.

of the HST is approximately 2 μm or 7 μm, as shown in Fig. 2 (a) and (c), the reflected light intensity from R1 is less or larger than that from R2. The large intensity difference between the two reflected light beams leads to low contrast ratio, as shown in Figs. 3(a) and 2(c), respectively. Furthermore, the low fusion intensity and short fusion time make the minimum inner diameters of the HST larger than the diameter of the optical fiber core, as shown in Fig. 2(d). Under these conditions, only a small amount of lights propagates into the HST, and the interference fringes are very weak and even vanish. The largest contrast ration of the interference fringe with 14 μm inner diameter is 1.2 dB, as shown in Fig. 3(d). The fringe contrast depends on the light intensity difference of two reflective parts [17], and the light intensity difference is determined by the minimum inner diameter of HST.

From Fig. 3, it can be seen that the free spectral range (FSR) of the interference fringes decreases as the HST length increases. The FSR of the FPI is given by

$$\text{FSR} = \frac{\lambda^2}{2nL} \tag{1}$$

where λ is the wavelength of light, n is the RI, and L is the HST length. According to Eq. (1), the theoretical relationship between the FSR around a wavelength of 1550 nm and L is shown in Fig. 4. Accordingly, FPIs with different L were fabricated to demonstrate their relationship. As illustrated in Fig. 4, the measured FSRs around 1550 nm agree well with the calculated results.

3. Experiment

In the experiment, we tested the FPI responses to temperature and RI. The experimental setup is illustrated in Fig. 5. We used the peak tracing method to demodulate the signal from the FPI. Temperature measurements were performed by placing an FPI sample with $L=571$ μm inside a controllable muffle furnace (Nabertherm, sn209012, Germany). The sample was held and protected by a stainless steel fixture. We increased the temperature from 25 °C to 900 °C in steps of 50 °C. The interference fringes were recorded at each step once the temperature was stabilized for 10 min. An interference fringe shift towards a longer wavelength, i.e., red shift, could be observed in the spectrum with increasing temperature, as shown in Fig. 6(a). The relationship between the fringe shift of a selected peak and the temperature is presented in Fig. 6(b). The experimental results were well fit by the second-order polynomial
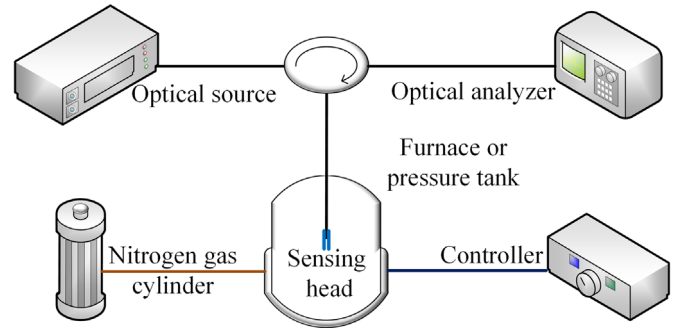

Fig. 4. Relationship between FSR and HST length.

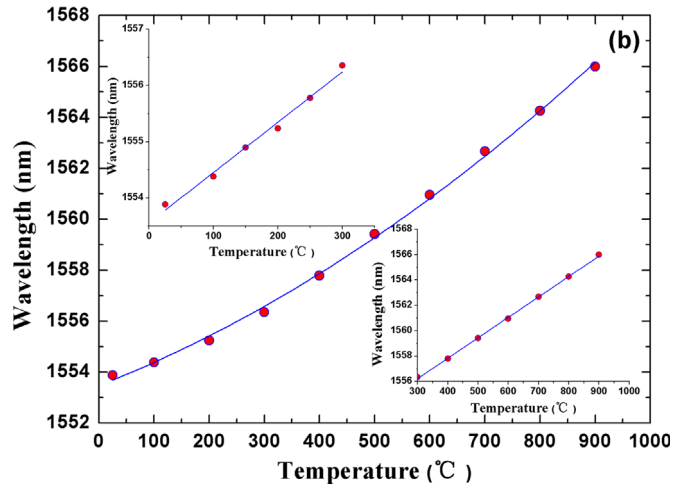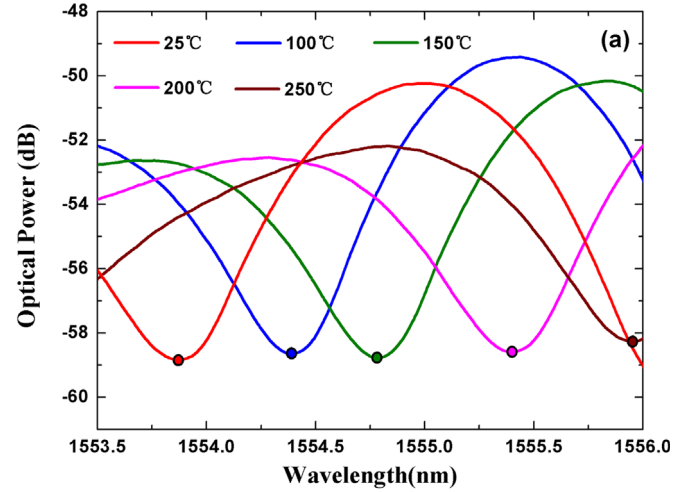**Fig. 5.** Experimental setup for temperature and refractive index test.

Fig. 6. Temperature response of sample FPI: (a) fringe shifts at temperatures from 25 °C to 250 °C, (b) relationship between fringe shift and temperature, where top left inset is low-temperature response, and bottom right inset is high-temperature response.

$$y = 1553.47 + 0.0085T + 6.21 \times 10^{-6}T^2 \tag{2}$$

The R^2 value of the fitting curve was 99.8%. However, it is reasonable to divide the temperature range into two different regions corresponding to high temperature (300–1000 °C) and low temperature (25–300 °C) (Fig. 6(b) insets), because a linear approximation can be used at high temperature but would not be sufficient at low temperature. The obtained sensitivities were 16.26 pm/°C and 8.94 pm/°C for the high and low temperature scenarios, respectively. This temperature response is caused by the thermal expansion of the material and the thermo-optic effect.
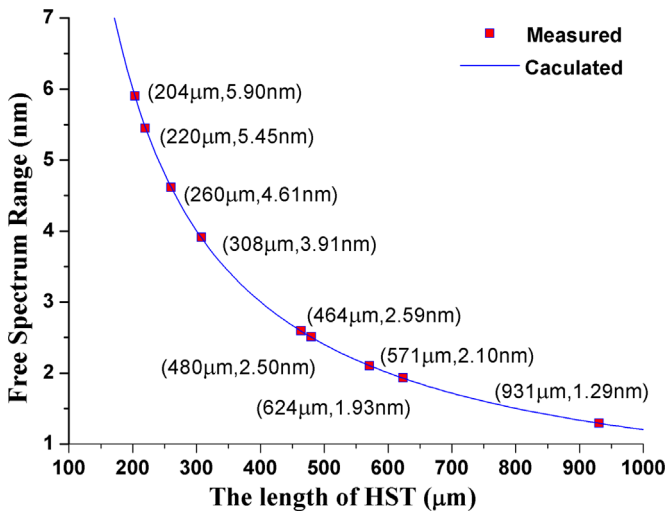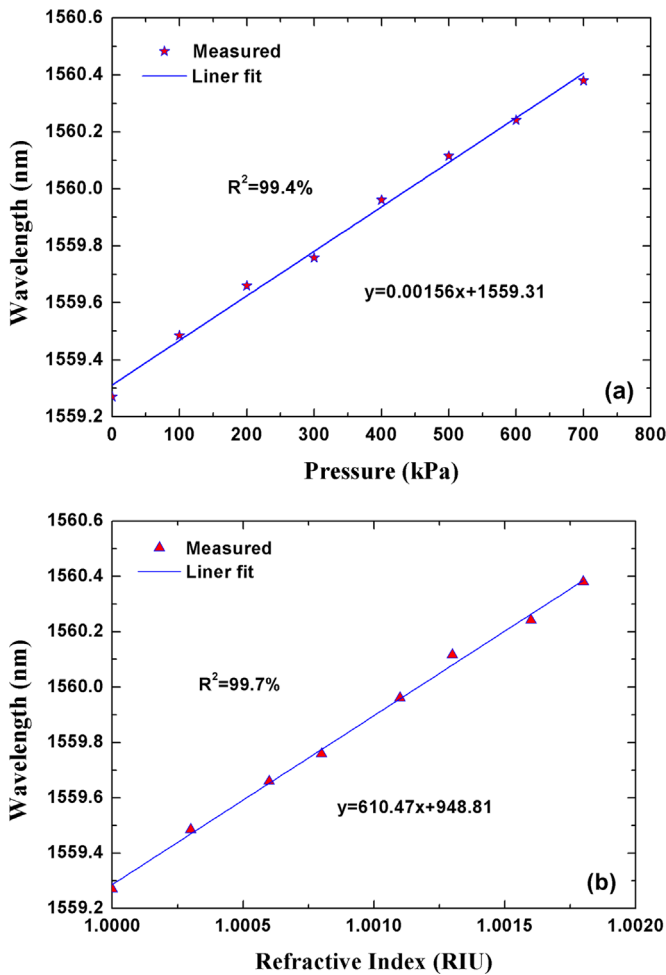
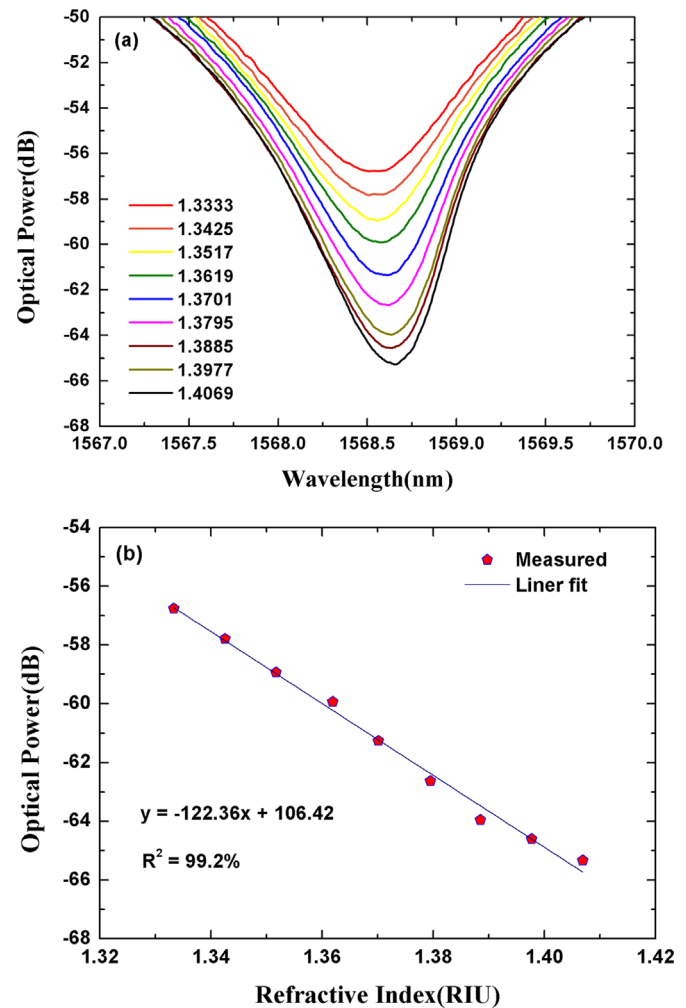Fig. 7. (a) Pressure and (b) RI responses of sample FPI.

Fig. 8. Liquid RI response of sample FPI: (a) optical power valley variation in different solutions, and (b) relationship between optical power and RI.

The different sensitivities in the low and high temperature ranges occur because the thermal expansion coefficient of SiO_2 varies when temperature changes [21,22].

The gas RI measurements were performed by placing the FPI sample with $L = 308$ μm inside a sealed chamber with a gas input and a vacuum output. The measurements covered a range of 700 kPa in steps of 100 kPa in a nitrogen atmosphere. Using the peak tracing method, a slight red shift of the interference fringes was observed with increasing pressure. Because the RI of a gas is related to the pressure at a given temperature [19], the fringe shift in response to the pressure reflects the RI. Fig. 7(a) and (b) show that the interference fringe shift is a function of RI or pressure, and the sensitivities to RI and pressure are 610.47 nm/RIU and 1.56 pm/kPa, respectively.

The FPI response to liquid RI was also investigated. A sample of this kind of FPI was vertically immersed into distilled water and was held submerged for 5 min. The resulting interference fringe was recorded. Then the sample was immersed into NaCl solutions with different concentrations. The concentrations of the solutions varied from 5% to 45% in steps of 5%, and the according RIs varied from 1.3426 to 1.4069. The relevant fringes are illustrated in Fig. 8 (a). According to Fig. 8(a), the optical power of the selected valley decreases with increasing liquid RI. The relationship between the optical power and the RI is shown in Fig. 8(b), which demonstrates that the FPI has a linear response to the liquid RI with a sensitivity of −122.36 dB/RIU.

4. Conclusion

In conclusion, we presented a diaphragm-free FPI fabricated by splicing an HST to an SMF and fusing the inner core of the HST to a taper. The interference fringes are influenced by the minimum inner diameters of the HST. The fabrication process is simple and could potentially be applied in low-cost batch fabrication. The experimental results demonstrated that the FPI is sensitive to temperature, gas RI, liquid RI and gas pressure. Thus, the FPI has great potential to be applied as a sensor for measuring temperature, RI or pressure.

References

[1] X. Zou, A. Chao, Y. Tian, N. Wu, H. Zhang, T. Yu, X. Wang, An experimental study on the concrete hydration process using Fabry–Perot fiber optic temperature sensors, Measurement 45 (2012) 1077–1082.
[2] C. Liao, S. Liu, L. Xu, C. Wang, Y. Wang, Z. Li, Q. Wang, D. Wang, Sub-micron silica diaphragm-based fiber-tip Fabry–Perot interferometer for pressure measurement, Opt. Lett. 39 (2014) 2827–2830.

[3] E. Cibula, D. Donlagic, In-line short cavity Fabry–Perot strain sensor for quasi distributed measurement utilizing standard OTDR, Opt. Express 15 (2007) 8719–8730.

[4] Y. Liu, S. Qu, Optical fiber Fabry–Perot interferometer cavity fabricated by femtosecond laser-induced water breakdown for refractive index sensing, Appl. Opt. 53 (2014) 469–474.

[5] W. Xu, W. Huang, X. Huang, C. Yu, A simple fiber-optic humidity sensor based on extrinsic Fabry–Perot cavity constructed by cellulose acetate butyrate film, Opt. Fiber Technol. 19 (2013) 583–586.

[6] P. Nieva, N. McGruer, G. Adams, Design and characterization of a micromachined Fabry–Perot vibration sensor for high-temperature applications, J. Micromech. Microeng. 16 (2006) 2618.

[7] T. Yoshino, K. Kurosawa, K. Itoh, T. Ose, Fiber-optic Fabry–Perot interferometer and its sensor application, IEEE J. Quantum Electron. 18 (1982) 1612–1621.

[8] H. Pang, H. Bae, A. Gupta, K. Bryden, M. Yu1, MEMS Fabry–Perot sensor interrogated by optical system-on-a-chip for simultaneous pressure and temperature sensing, Opt. Express 21 (2013) 21829–21839.

[9] M. Ferreira, J. Bierlich, S. Unger, K. Schuster, J. Santos, O. Frazao, Post-processing of Fabry–Perot microcavity tip sensor, IEEE Photon. Technol. Lett. 25 (2013) 1593–1596.

[10] D. Duan, Y. Rao, Y. Hou, T. Zhu, Microbubble based fiber-optic Fabry–Perot interferometer formed by fusion splicing single-mode fibers for strain measurement, Appl. Opt. 51 (2012) 1033–1036.

[11] F. Favero, G. Bouwmans, V. Finazzi, J. Villatoro, V. Pruneri, Fabry–Perot interferometers built by photonic crystal fiber pressurization during fusion splicing, Opt. Lett. 36 (2011) 4191–4193.

[12] J. Tian, Y. Lu, Q. Zhang, M. Han, Microfluidic refractive index sensor based on an all-silica in-line Fabry–Perot interferometer fabricated with microstructured fibers, Opt. Express 21 (2013) 6633–6639.

[13] R. Wang, X. Qiao, Gas Refractometer Based on Optical Fiber Extrinsic Fabry–Perot Interferometer With Open Cavity, IEEE Photon. Technol. Lett. 27 (2015) 245–248.

[14] S. Liu, Y. Wang, C. Liao, G. Wang, Z. Li, Q. Wang, J. Zhou, K. Yang, X. Zhong, J. Zhao, J. Tang, High-sensitivity strain sensor based on in-fiber improved Fabry–Perot interferometer, Opt. Lett. 39 (2014) 2121–2124.

[15] S. Wu, G. Yan, B. Zhou, E. Lee, S. He, Open-Cavity Fabry-Perot Interferometer Based on Etched Side-Hole Fiber for Microfluidic Sensing, IEEE Photon. Technol. Lett. 27 (2015) 1813–1816.

[16] S. Wu, G. Yan, Z. Lian, X. Chen, B. Zhou, S. He, An open-cavity Fabry-Perot interferometer with PVA coating for simultaneous measurement of relative humidity and temperature, Sens. Actuators B 225 (2016) 50–56.

[17] Z. Huang, X. Chen, Y. Zhu, A. Wang, Wavefront splitting intrinsic Fabry-Perot fiber optic sensor, Opt. Eng. 44 (2005) 1–3.

[18] M.S. Ferreira, L. Coelho, K. Schuster, J. Kobelke, J.L. Santos, O. Frazao, Fabry–Perot cavity based on a diaphragm-free hollow-core silica tube, Opt. Lett. 36 (2011) 4029–4031.

[19] S. Silva, L. Coelho, O. Frazao, An all-fiber Fabry–Perot interferometer for pressure sensing in different gaseous environments, Measurement 47 (2014) 418–421.

[20] R. Wang, X. Qiao, Intrinsic Fabry–Perot interferometer based on concave well on fiber end, IEEE Photon. Technol. Lett. 26 (2014) 1430–1433.

[21] J. Mathew, O. Schneller, D. Polyzos, D. Havermann, R. Carter, W. MacPherson, D. Hand, R. Maier, In-Fiber Fabry–Perot cavity sensor for high-temperature applications, J. Light. Technol. 33 (2015) 2419–2425.

[22] J. Wang, B. Dong, E. Lally, J. Gong, M. Han, A. Wang, Multiplexed high temperature sensing with sapphire fiber air gap-based extrinsic Fabry–Perot interferometers, Opt. Lett. 35 (2010) 619–621.